

## Tailoring Optical Properties of Atomically-Thin WS<sub>2</sub> via Ion Irradiation

Tan, L. N.; Tan, Y.; Ghorbani-Asl, M.; Boettger, R.; Kretschmer, S.; Zhou, S. Q.;  
Huang, Z. Y.; Krasheninnikov, A. V.; Chen, F.;

Originally published:

August 2017

**Nanoscale 9(2017)31, 11027-11034**

DOI: <https://doi.org/10.1039/C7NR02025B>

Perma-Link to Publication Repository of HZDR:

<https://www.hzdr.de/publications/Publ-25650>

Release of the secondary publication  
on the basis of the German Copyright Law § 38 Section 4.



## Tailoring Optical Properties of Atomically-Thin WS<sub>2</sub> via Ion Irradiation

L. N. Ma,<sup>a</sup> Y. Tan,<sup>a\*</sup> M. Ghorbani-Asl,<sup>b</sup> R. Boettger,<sup>b</sup> S. Kretschmer,<sup>b</sup> S. Q. Zhou,<sup>b</sup> Z. Y. Huang,<sup>c</sup> A. V. Krasheninnikov<sup>b,d</sup> and F. Chen<sup>a</sup>

Received 00th January 20xx,  
Accepted 00th January 20xx

DOI: 10.1039/x0xx00000x

www.rsc.org/

Two-dimensional transition metal dichalcogenides (TMDCs) exhibit excellent optoelectronic properties. However, the large band gaps in many semiconducting TMDCs make optical absorption in the near-infrared (NIR) wavelength regime impossible, which prevents applications of these materials in optical communications. In this work, we demonstrate that Ar<sup>+</sup> ion irradiation is a powerful post-synthesis technique to tailor the optical properties of the semiconducting tungsten disulfide (WS<sub>2</sub>) by creating S vacancies and thus controlling material stoichiometry. First-principles calculations reveal that the S-vacancies give rise to deep states in the band gap, which determine the NIR optical absorption of the WS<sub>2</sub> monolayer. As the density of the S-vacancies increases, the enhanced NIR linear and saturable absorption of WS<sub>2</sub> is observed, which is explained by the results of first-principles calculations. We further demonstrate that by using the irradiated WS<sub>2</sub> as a saturable absorber in a waveguide system, the passively Q-switched laser operations can be optimized, opening thus new avenues for tailoring the optical response of TMDCs by defect-engineering through ion irradiation.

### Introduction

Two-dimensional (2D) transition metal dichalcogenides (TMDCs) have attracted large amount of attention due to their unique optoelectronic and electrocatalytic properties.<sup>1-8</sup> Unlike semi-metallic graphene, many members of the TMDC family have band gaps, which leads to a broad and strong absorption in spectrum range from ultra-violet to visible (UV-Vis).<sup>9-11</sup> This feature indicates the great potential of TMDCs for photocatalysis, solar cells and high-responsivity UV-Vis photodetector applications.<sup>12-16</sup> Pristine WS<sub>2</sub> has little absorption in the NIR region due to its large band gap<sup>17-20</sup>, limiting its application in optical communications. One of the effective solutions to overcome this difficulty is to implement defect engineering in TMDCs, by which defect-associated states or even narrow bands may be produced in the band gap if the concentration of defects is high enough.

When S-vacancies are present, WS<sub>2</sub> exhibits significantly

enhanced NIR optical absorption responses in comparison to graphene under similar excitation condition.<sup>21-25</sup> Vacancies and other defects in the WS<sub>2</sub> monolayer can be produced during the fabrication process, but it is rather difficult to control the density of defects. Ion irradiation is a well-established method to create atomic-scale defects in 2D materials.<sup>26-32</sup> During the irradiation process, the incident energetic ions collide with the atoms in WS<sub>2</sub>, leading to their displacements. Motivated by the requirements for possible optical applications in the NIR regime, we study how the irradiation-induced atomic-scale defects affect optical properties of WS<sub>2</sub>. By combining NIR, XPS and Raman spectroscopy with first-principles calculations, we show that S-vacancy concentration and optical properties of WS<sub>2</sub> can be modified in a controllable way via ion irradiation. The NIR saturable absorption of the WS<sub>2</sub> monolayer is enhanced after ion irradiation due to the intermediate states induced by S-vacancies. We have also used the irradiated WS<sub>2</sub> monolayer as a successful saturable absorber in a waveguide system to obtain optimized Q-switching lasing.

### Results and discussion

#### WS<sub>2</sub> stoichiometry tailored by ion irradiation.

<sup>a</sup> School of Physics, State Key Laboratory of Crystal Materials, Shandong University, Jinan 250100, China. E-mail: tanyang@sdu.edu.cn

<sup>b</sup> Institute of Ion Beam and Materials Research, Helmholtz-Zentrum Dresden-Rossendorf, Bautzner Landstrasse, 400, 01328 Dresden, Germany.

<sup>c</sup> Hunan Key Laboratory of Micro-Nano Energy Materials and Devices, Laboratory for Quantum Engineering and Micro-Nano Energy Technology and School of Physics and Optoelectronics, Xiangtan University, Xiangtan, 411105, People's Republic of China.

<sup>d</sup> Department of Applied Physics, Aalto University, P.O. Box 11100, FI-00076 Aalto, Finland.

† Electronic supplementary information (ESI) available: Here, you will find XPS spectra of as-prepared and irradiated WS<sub>2</sub>, TEM images of as-prepared and irradiated WS<sub>2</sub>, Q-switched lasing based on Yb:YAG waveguide cavity, Measurement of the imaginary refractive index of WS<sub>2</sub>. See DOI: 10.1039/x0xx00000x

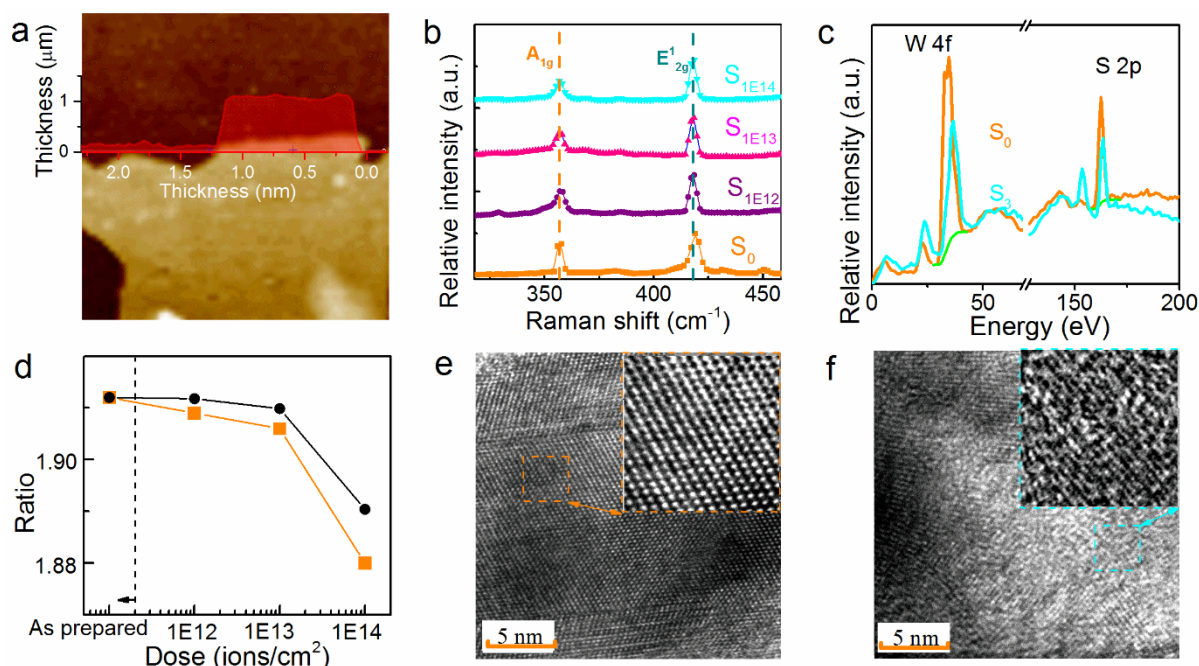


Fig. 1 (a) Morphology of the as-prepared WS<sub>2</sub> monolayer captured by the AFM. And the thickness of the WS<sub>2</sub> along the Red line in (a). (b) The Raman spectra of the as-prepared (S<sub>0</sub>) and the irradiated (S<sub>1E12</sub>, S<sub>1E13</sub>, S<sub>1E14</sub>) WS<sub>2</sub> monolayers. (c) The XPS spectra of the S<sub>0</sub> and S<sub>3</sub>. (d) The measured (orange squares) and calculated (black circles) variation of the atomic ratio (S/W) as a function of irradiation dose. TEM image of the as-prepared (e) and the irradiated (f) WS<sub>2</sub> monolayer.

The WS<sub>2</sub> monolayer samples used in this work were prepared on the Al<sub>2</sub>O<sub>3</sub> wafer by the chemical vapor deposition (CVD) method. We ascertained the monolayer nature of our samples by atomic force microscopy (AFM) and Raman measurements. As shown in Fig. 1a, the AFM measurements reveal the height of ~ 0.8 nm corresponding to the thickness of a single unit cell. WS<sub>2</sub> monolayers are irradiated by Ar<sup>+</sup> ion beam at energy of 60 keV with controlled dose/fluence (S<sub>1E12</sub> = 1 × 10<sup>12</sup> ions/cm<sup>2</sup>; S<sub>1E13</sub> = 1 × 10<sup>13</sup> ions/cm<sup>2</sup> and S<sub>1E14</sub> = 1 × 10<sup>14</sup> ions/cm<sup>2</sup>) to create different densities of point defects. The Raman spectra of the as-prepared monolayer (S<sub>0</sub>) and the irradiated ones (with doses S<sub>1E12</sub>, S<sub>1E13</sub> and S<sub>1E14</sub>) are displayed in Fig. 1b. The two characteristic peaks corresponding to the E<sub>2g</sub><sup>1</sup> mode (in-plane vibration of tungsten and sulfur atoms) and the A<sub>1g</sub> mode (the out-of-plane vibrations of the sulfur atoms) are observed in all films. The peak positions of A<sub>1g</sub> and E<sub>2g</sub><sup>1</sup> are 356.7 and 418.45 cm<sup>-1</sup>, respectively, which agree with other reports.<sup>33</sup> Moving from the as-prepared monolayer (S<sub>0</sub>) to the irradiated ones (S<sub>1E12</sub>, S<sub>1E13</sub>, S<sub>1E14</sub>), the intensity ratio of A<sub>1g</sub>/E<sub>2g</sub><sup>1</sup> of the WS<sub>2</sub> monolayer gradually decreases from 0.76 to 0.50 with increasing the dose of the incident ion beam. It means that the out-of-plane vibrations of the S atoms (the A<sub>1g</sub> mode) are changed by ion irradiation. The chemical states of the S atoms in the monolayers are further investigated by X-ray photoelectron spectroscopy (XPS), with the results being shown in Fig. 1c (see Part I in supplement). The evolution of the atomic ratio is presented in Fig. 1d (orange squares). The as-prepared WS<sub>2</sub> has the stoichiometric ratio of S:W ~1.92, which suggests that the atomic structure of the as-prepared WS<sub>2</sub> is not perfect. After ion irradiation, the S:W atomic ratio decreases to 1.88. It implies that the incident ion beam creates

S-vacancies in the WS<sub>2</sub> monolayer, and the ratio of the S and W atoms can be controlled by the dose of the incident ion beams. The transmission electron microscope images of the as-prepared and irradiated (S<sub>1E14</sub>) WS<sub>2</sub> monolayer are shown in Fig. 1e and 1f, which demonstrate that the deficiency of S atoms gives rise to the vacancies, but not to the appearance of mirror twin boundaries, as reported for MoSe<sub>2</sub>.<sup>34</sup>

In order to provide an accurate and detailed description of ion impacts onto WS<sub>2</sub>, we have performed classical molecular dynamics (MD) simulations of ion irradiation of WS<sub>2</sub> monolayers. The simulation setup is illustrated in Fig. 2a. We consider low-dose irradiation, in which the incremental effects of the impacts into the same lattice area are negligible. The simulations have been carried out for 32 energies ranging from 10 eV to 1 MeV. Similar to the behaviour of other 2D materials, e.g., graphene<sup>35</sup> and MoS<sub>2</sub><sup>36</sup> under ion bombardment, the sputtering yield first increases with energy up to a peak value (~530 eV) and then drops with ion energy due to a smaller cross section for ballistic energy transfer at high energies (see Fig. 2b). In order to assess the effects of substrate corrugation (and thus possible off-normal incidence of the ion beam on the WS<sub>2</sub> monolayer) on defect production in WS<sub>2</sub>, we have also studied the sputtering yield as a function of incident angle (θ). The results show that the sputtering yield is almost invariant at small incident angles, i.e. θ < 10°, as shown in Fig. 2c. Therefore, we expect no significant changes in the results due to the roughness of the monolayer. We stress that the substrate may affect defect production, as compared to the free-standing system considered in our simulations.<sup>37</sup> As, on the one hand, the substrate can decrease forward sputtering yield and increase defect annealing, while on the other hand

the free-standing monolayer is not damaged by the backscattered ions and sputtered substrate atoms, we assume that, to the first order, the effects of substrate cancel each other, and the results for the freestanding monolayer are qualitatively correct for the supported system.

(1)

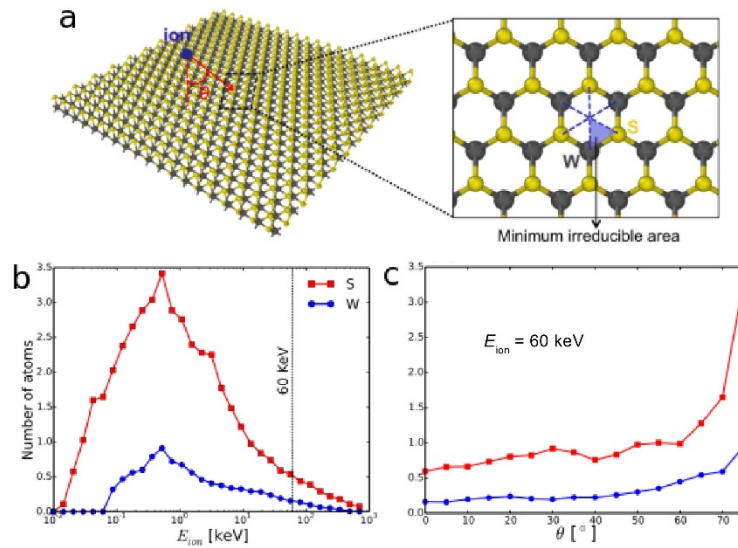
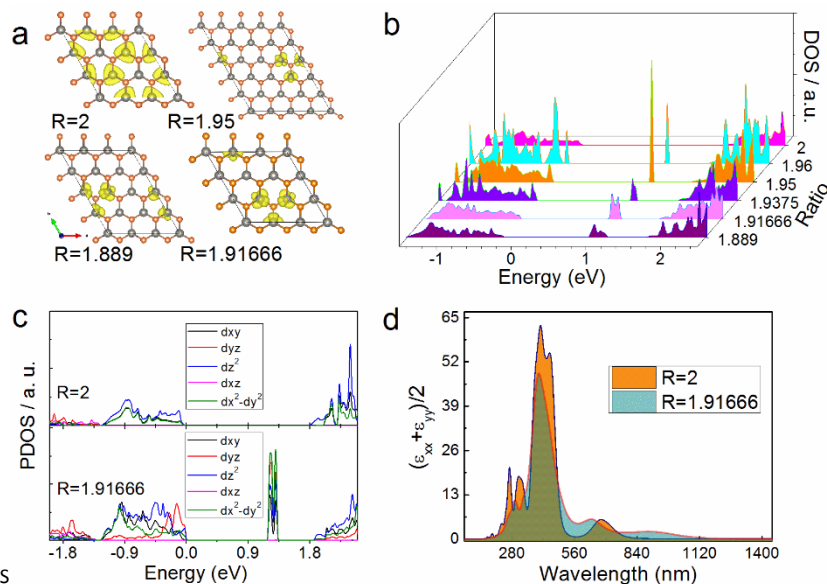


Fig. 2 (a) Left: Schematic representation of the setup used for ion irradiation simulations of WS<sub>2</sub> monolayer. The incident angle has been indicated by  $\theta$ . Tungsten and sulfur atoms are shown in gray and yellow, respectively. Right: The blue triangle represents the minimum irreducible area for ion impacts. (b) Average numbers of sputtered atoms in WS<sub>2</sub> monolayer as functions of ion energy and (c) incident angle for Ar<sup>+</sup> ion beams.

In this work, energetic Ar ions are normally incident ( $\theta = 0$ ) onto the WS<sub>2</sub> monolayer with the energy of 60 keV. As shown in Fig. 2b, every ten incident Ar ions sputter 5 S ions and 1 W ion off the WS<sub>2</sub> monolayer. The loss of S ions is faster than W ions, demonstrating the decreasing of the atomic ratio (S:W). We calculated the variation of the atomic ratio of the WS<sub>2</sub> monolayer after ion irradiation ( $R_n$ ,  $n$  corresponding to the subscript of  $S_{1E12}$ ,  $S_{1E13}$  and  $S_{1E14}$ ) using a simple empirical formula:

$$R_n = \frac{\frac{D}{R_0 + 1} - F \times 0.5}{\frac{R_0 \times D}{R_0 + 1} - F \times 0.1}$$

where  $D$  is the atomic density of the WS<sub>2</sub> monolayer ( $4.312 \times 10^{15}$  atoms/cm<sup>2</sup>),  $F$  is the dose of Ar ion beam,  $R_0$  is the S:W atomic ratio in the as-prepared sample. Fig. 1d (black circles) shows the variation of the atomic ratio of monolayer WS<sub>2</sub> as a function of the ion dose. The atomic ratio is changed from 1.92 to 1.89 with increasing ion dose. As compared to the experimental results shown in Fig. 1d, the variation trend of the estimated ratio is in a good agreement with the measurement.



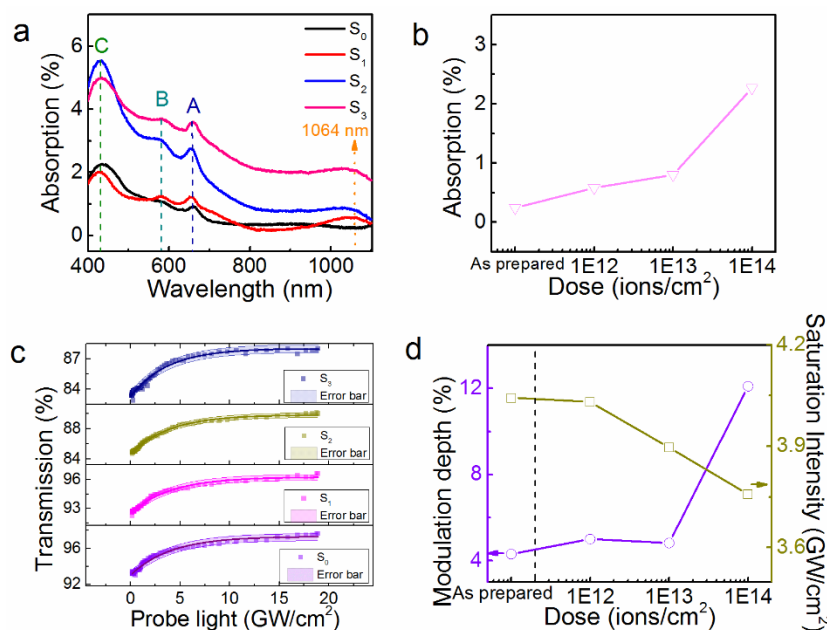


Fig. 4 (a) Linear absorption spectra of the as-prepared ( $S_0$ ) and the irradiated ( $S_{1E12}$ ,  $S_{1E13}$ ,  $S_{1E14}$ ) WS<sub>2</sub> monolayers. (b) Variation of the linear absorption at 1064 nm as a function of irradiation dose. (c) Nonlinear transmission of the WS<sub>2</sub> monolayers. Solid lines are fitted curves. (d) The evolution of the modulation depth and the saturation intensity along with increasing irradiation dose.

To understand the relationship between the S-vacancy density and the electronic structure of WS<sub>2</sub>, first-principles calculations were carried out. As displayed in Fig. 3a, the atomic ratios (R: the ratio of S and W atoms) in the WS<sub>2</sub> monolayer were set to be 2, 1.96, 1.96, 1.9375, 1.91666 and 1.889, respectively by choosing the appropriate size of the supercell with vacancies. Fig. 3b shows the densities of states (DOS) of WS<sub>2</sub> with different concentrations of S-vacancies. In the pristine material (R=2), the band gap of the WS<sub>2</sub> is 1.87 eV. After introducing S-vacancies into the monolayer (R=1.91666), the mid-gap states appear. Fig. 3c shows the atomic orbital-resolved electron density of states with (R=1.91666) and without S-vacancies. This indicates that the mid-gap states in the WS<sub>2</sub> monolayer are attributed to the d(xy) and d(x<sup>2</sup>-y<sup>2</sup>) atomic orbitals of the transition metal atoms.

Upon changing atom ratios between 2 and 1.899, the position of the adsorption peak is shifted from 1.87 eV to 1.01 eV. This allows for the optical absorption of WS<sub>2</sub> in the NIR region. In order to assess how the presence of S vacancies affects optical absorption, we calculate the complex dielectric function  $\epsilon$  of the WS<sub>2</sub> monolayer with S-vacancies, which can be expressed as

$$\epsilon(\omega) = \epsilon_1(\omega) + i\epsilon_{\alpha\beta}(\omega) \quad (2)$$

$$\epsilon_{\alpha\beta}(\omega) = \frac{4\pi^2 e^2}{\Omega} \lim_{q \rightarrow 0} \frac{1}{q^2} \sum_{c,v,k} 2w_k - \delta(\epsilon_{ck} - \epsilon_{vk} - \omega) \times \langle u_{\bar{c}k+\beta\alpha q} | u_{v,\bar{k}} \rangle \langle u_{\bar{c}k+\alpha\beta q} | u_{v,\bar{k}} \rangle \quad (3)$$

where  $\epsilon_{\alpha\beta}$  is the imaginary part;  $\alpha$  and  $\beta$  represent the x, y, or z coordinates; c and v refer to the conduction and valence band states, respectively;  $u_{c,k}$  corresponds to the cell periodic part of the wave functions at the k-point. According to the electric

field polarization (along or perpendicular to the z-direction),  $\epsilon_{\alpha\beta}(\omega)$  is decomposed into  $\epsilon_{zz}(\omega)$  and  $(\epsilon_{xx}(\omega) + \epsilon_{yy}(\omega))/2$ . As light passing through the WS<sub>2</sub> monolayer has a transverse wave with a polarization parallel to the monolayer, we only consider  $(\epsilon_{xx}(\omega) + \epsilon_{yy}(\omega))/2$  in this work. Fig. 3d shows the imaginary part  $(\epsilon_{xx}(\omega) + \epsilon_{yy}(\omega))/2$  for the monolayer WS<sub>2</sub> with and without S-vacancy (R=1.91666). As compared to the pristine monolayer, WS<sub>2</sub> with S-vacancies has additional optical absorption in the near-infrared range, being attributed to the presence of mid-gap states.

#### Tailored optical properties of the monolayer WS<sub>2</sub>.

Fig. 4a shows the evolution of the linear absorption spectrum of the WS<sub>2</sub> monolayer with increasing irradiation dose. The positions of A and B exciton peaks at ~658 and ~581 nm do not change, but a large increase in absorption is observed in the NIR wavelength range in the irradiated monolayers. The enhanced absorption agrees with the results of the electronic structure calculation presented in Fig. 3d. S-vacancies created by the irradiation increase the density of mid-gap states, which induces the absorption of the NIR light. Fig. 4b displays the variation of the linear absorption at the wavelength of 1064 nm as a function of ion dose, which has an obvious increasing. The linear optical absorption of the WS<sub>2</sub> in the NIR region can be well tailored by ion irradiation.

The nonlinear absorption of the WS<sub>2</sub> monolayers is detected by the Z-scan technology at the wavelength of 1064 nm. Measured nonlinear transmissions are shown in Fig. 4c. The modulation depth ( $\Delta T$ ) and the saturable intensity ( $I_{\text{sat}}$ ) of WS<sub>2</sub> monolayers are quantitatively determined by the equation below:

$$T(I) = 1 - \Delta T \times e^{-\frac{I}{I_{\text{sat}}}} - T_N \quad (4)$$

where  $T_N$  is the non-saturable absorbance,  $T$  and  $I$  are the transmission and the excitation energy, respectively. Fitted values of  $\Delta T$  and  $I_{\text{sat}}$  are shown in Fig. 4d as a function of the dose. With increasing ion dose, the modulation depth increases and the saturable intensity decreases. These changes demonstrate two advantages of the irradiated  $\text{WS}_2$  monolayer: 1) For the Q-switched pulsed laser, the pulse duration of the laser is inversely proportional to the modulation depth. The increased modulation depth allows for the application potential for a shorter pulsed laser. 2) The saturation intensity of the  $\text{WS}_2$  is decreased after irradiation. Therefore, a lower energy of the excitation laser is required for the pulsed lasing.

### Q-switched pulses

TAs shown in the above-mentioned section, the saturable absorption of  $\text{WS}_2$  can be quantitatively modified by ion

calculate the modulation depth of the as-prepared  $\text{WS}_2$  monolayer by the following equation<sup>38</sup>:

$$\tau_p \approx \frac{3.53T_R}{\Delta R} \quad (5)$$

where  $\Delta R$  is the modulation depth,  $\tau_p$  is the pulse duration, and  $T_R$  is the cavity round-trip time. The evolution of the modulation depth is shown in Fig. 5e. The maximum modulation depth of the irradiated  $\text{WS}_2$  monolayer is calculated to be 0.42%, corresponding to the pulse duration of 265 ns.

Using the irradiated ( $S_{1E13}$ ,  $S_{1E14}$ )  $\text{WS}_2$  monolayer as the saturable absorber, the pulsed laser emission is also observed at the wavelength of 1064 nm. The output power, the pulse train, pulse duration and modulation depth of the pulsed laser are illuminated in Fig. 5b, 5c, 5d and 5e, respectively. The lasing threshold of the pulsed laser is decreased (88 mW  $S_{1E13}$ ,

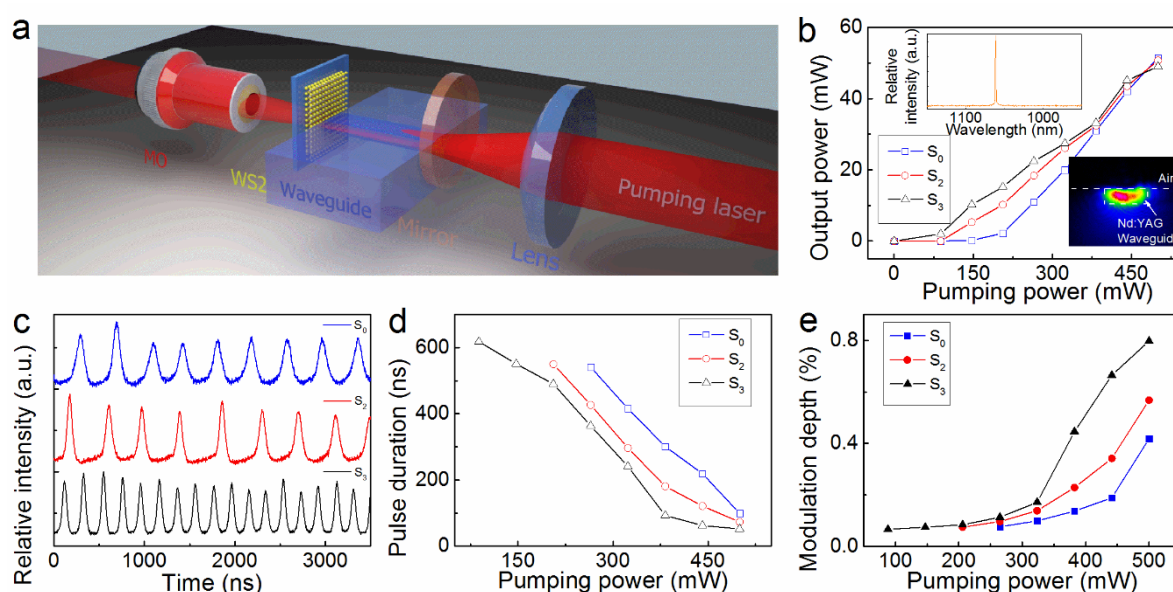


Fig. 5 (a) Experimental setup for the Q-switched pulsed waveguide lasing. The output power (b), pulse trains (c), pulse duration (d) and modulation depth (e) of the output laser modulated by the as-prepared ( $S_0$ ) or irradiated ( $S_{1E13}$ ,  $S_{1E14}$ )  $\text{WS}_2$  monolayer. MO: Microscope objective.

irradiation. Here, we demonstrate how to utilize the irradiated  $\text{WS}_2$  monolayer as a saturable absorber to optimize the Q-switched pulses. For this purpose, the as-prepared and the irradiated  $\text{WS}_2$  wafers are used as the saturable absorbers in a waveguide laser cavity, respectively. The experimental setup for the passively Q-switched laser emission is shown in Fig. 5a. Utilizing the as-prepared ( $S_0$ )  $\text{WS}_2$  as a saturable absorber, the pulsed laser emission at the wavelength of 1064 nm is observed (inset in Fig. 5b) corresponding to the laser threshold of 120 mW. The average output power as a function of the incident pumping power is illustrated in Fig. 5b. The output power has a linear variation along with the increasing of the pumping power with a maximum output power of 52 mW. Fig. 5c illustrates the evolution of the pulse duration as a function of the pumping power. By increasing the pumping power, the pulse duration of the output laser gradually decreases from 500 ns to 265 ns. Based on the measured pulse duration, we

70 mW  $S_{1E14}$ ), and the maximum output power is around 50 mW. The minimum pulse duration gradually is decreased (72.9 ns  $S_{1E13}$ , 52 ns  $S_{1E14}$ ) with the increasing of doses. The maximum modulation depth is 0.8%. Compared with the as-prepared  $\text{WS}_2$ , two conclusions can be deduced: 1) The pulsed laser modulated by the irradiated  $\text{WS}_2$  has a lower laser threshold. 2) The modulation depth of the irradiated  $\text{WS}_2$  monolayer is higher than that of the as-prepared one. The function of the pulsed waveguide laser can be optimized on demand by using the irradiated  $\text{WS}_2$  monolayer as the saturable absorber.

### Conclusions

We have demonstrated that ion irradiation is a powerful technique to tailor optical properties of the atom-thin  $\text{WS}_2$  monolayers. S-vacancies in the  $\text{WS}_2$  monolayer create mid-gap states, resulting in the enhanced saturable absorption in the NIR region. In general, S-vacancies can be produced via the

hydrolysis reaction with water during the fabrication process, such as  $S^{2-} + 2H_2O \rightarrow H_2S + 2OH^-$ . However, the concentration of the S-vacancies in  $WS_2$  monolayers can hardly be controlled via this reaction, contrary to ion beam irradiation, which makes it possible to tailor optical properties. Using the irradiated  $WS_2$  monolayer as a saturable absorber, we have fabricated a Q-switched pulsed laser from a Nb:YAG ceramic waveguide. Compared with the as-prepared  $WS_2$ , the performance of the Q-switched laser was enhanced considerably. This work demonstrates that 2D materials can be efficiently modified by ion irradiation, therefore creating a new dimensionality for photonic applications.

## Methods

### Ion irradiation

Four pieces of  $WS_2$  monolayers were prepared for this work under the same fabrication conditions. Three of them were irradiated by  $Ar^+$  ions at the energy of 60 keV at doses of  $1 \times 10^{12}$  ions/cm<sup>2</sup>,  $1 \times 10^{13}$  ions/cm<sup>2</sup> and of  $1 \times 10^{14}$  ions/cm<sup>2</sup> (labelled as  $S_{1E12}$ ,  $S_{1E13}$  and  $S_{1E14}$ ), respectively.

### Z-scan measurement

The nonlinear absorption of the  $WS_2$  monolayer was measured by the single-beam Z-scan technology. During the measurement, a 1064-nm laser with a 4-ns pulse duration and an energy of 1  $\mu$ J was focused by a lens (a focal distance of 400 mm). The beam waist of the detecting light was  $\sim 24.5$   $\mu$ m. A large-aperture lens was used to collect the transmitted laser light. Translating the samples around the focal point, the power of the transmitted light was measured as a function of the distance from the focal point.

### First principles calculations

We carried out the ab initio calculations of the  $WS_2$  monolayer using density-functional theory (DFT) with a projector augmented wave method and the Perdew-Burke-Ernzerhof (PBE) type generalized gradient approximation as implemented in the Vienna ab initio simulation package (VASP). The energy precision of the plane waves was set to be  $1 \times 10^{-6}$  eV, with the kinetic energy cutoff of 700 eV. The Brillouin zone was sampled using  $\Gamma$ -centered Monkhorst–Pack grids with  $11 \times 11 \times 1$ . We optimized the atomic positions and the lattice vectors by the conjugate gradient (CG) scheme without any symmetric restriction until the maximum force on each atom less than 0.001 eV $\text{\AA}^{-1}$ . Although DFT calculations with local and semilocal exchange and correlation functions are known to underestimate the fundamental band gap and affect the positions of defect-associated levels in the electronic spectrum, electronic structure calculations for large supercells with defects using more rigorous GW approximation are beyond our reach due to high computational cost and memory requirements of such calculations. For that same reason, we did not explicitly account for exciton binding energies. Although they can be large in freestanding 2D systems<sup>39-41</sup>, the presence of the substrate reduces binding energy due to

additional screening<sup>40,42</sup>, so that our calculations should provide at least qualitatively correct picture.

### Molecular dynamic simulations

All the molecular dynamic simulations have been carried out using the large-scale atomic/molecular massive parallel simulator (LAMMPS) code.<sup>43</sup> Periodic boundary conditions are applied to the 2D plane of  $WS_2$ . Atomic interactions through the  $WS_2$  monolayer were described by Stillinger-Weber (SW) potential<sup>44</sup> and the interaction between Ar and the monolayer atoms was described by the Ziegler-Biersack-Littmark (ZBL) universal repulsive potential<sup>45</sup>. To accurately model the interaction between S and W atoms in the collisional cascades, we smoothly joined the SW and ZBL potentials at small separations, as done previously<sup>46</sup>. We note that the SW potential was originally developed for  $MoS_2$ , but taking into account the very similar physical and chemical properties of these two systems, we used it for  $WS_2$  by simply changing the atom mass of metal atoms. The ion irradiation simulations were performed using a rectangular supercell containing 1254 atoms. Impact points were uniformly selected via 325 sites within the minimum irreducible area of the lattice. In order to properly simulate the evolution of the atomic structure and distribution of energy after the impact, the temperature of the irradiated sample was quenched after ion impact to about 1 K during a time period of 8 ps using a Nosé-Hoover thermostat. The results were obtained by analysing statistics over 10400 independent simulations for each incidence angle.

### Q-switched lasing in the waveguide cavity

The Q-switched lasing with ion irradiated  $WS_2$  as saturable absorber was implemented in a waveguide system.<sup>47</sup> A neodymium doped ytterbium aluminium garnet (Nb:YAG) ceramic waveguide produced by ion irradiation was used as the gain medium. The detailed information about the Nb:YAG waveguide has been reported in Ref.[48]. The input and output facets of the waveguide were covered by a mirror (high reflectivity at 1064 nm and a high transmission at 810 nm) and the  $WS_2$  monolayer, respectively. The mirror, the waveguide and the  $WS_2$  monolayer constituted a typical Fabry-Perot resonator for the laser oscillation. A continuous-wave laser at the wavelength of 810 nm was utilized as the pumping laser. Focused by a lens (focal length = 20 mm), the pumping laser was coupled into the waveguide. The output light from the waveguide was collected by a long-working-distance microscope objective ( $\times 20$ ) and detected by a fast photodetector (DET10A/M, Thorlabs, Inc., USA).

## Acknowledgements

This work is carried out with the financial support by the National Natural Science Foundation of China (No. 11535008). SZ acknowledges the financial support from the Helmholtz-Association (VH-NG-713). YT thanks the Young Scholars Program of Shandong University (Grant No. 2015WLJH20). AVK further thanks the Academy of Finland for the support under Project No. 286279.

## Notes and references

- M. Chhowalla, H. S. Shin, G. Eda, L.-J. Li, K. P. Loh and H. Zhang, *Nat. Chem.*, 2013, **5**, 263–275.
- Q. H. Wang, K. Kalantar-Zadeh, A. Kis, J. N. Coleman and M. S. Strano, *Nat. Nanotechnol.*, 2012, **7**, 699–712.
- G. Autès, D. M. Gresch, A. A. Troyer, Soluyanov and O. V. Yazyev, *Phys. Rev. Lett.*, 2013, **117**, 066402.
- T. F. Jaramillo, K. P. Jørgensen, J. Bonde, J. H. Nielsen, S. Hørch and I. Chorkendorff, *Science*, 2007, **317**, 100–102.
- O. V. Yazyev and S. G. Louie, *Nat. Mater.*, 2010, **9**, 806.
- E. Gruber, R. A. Wilhelm, R. Pétuya, V. Smejkal, R. Kozubek, A. Hierzenberger, B. C. Bayer, I. Aldazabal, A. K. Kazansky, F. Libisch, A. V. Krasheninnikov, M. Schleberger, S. Facsko, A. G. Borisov, A. Arnau and F. Aumayr, *Nat Commun.*, 2016, **7**, 13948.
- F. Herziger, C. Tyborski, O. Ochedowski, M. Schleberger and J. Maultzsch, *Phys. Rev. B*, 2014, **90**, 245431.
- F. Gargiulo and O. V. Yazyev, *Nano Lett.*, 2014, **14**, 250.
- N. Scheuschner, O. Ochedowski, A.-M. Kaulitz, R. Gillen, M. Schleberger and J. Maultzsch, *Phys. Rev. B*, 2014, **89**, 125406.
- A. Kuc, N. Zibouche and T. Heine, *Phys. Rev. B*, 2011, **83**, 245213.
- T. Georgiou, R. Jalil, B. D. Belle, L. Britnell, R. V. Gorbachev, S. V. Morozov, Y. Kim, A. Gholinia, S. J. Haigh, O. Makarovskiy, L. Eaves, L. A. Ponomarenko, A. K. Geim, K. S. Novoselov and A. Mishchenko, *Nat. Nanotechnol.*, 2013, **8**, 100–103.
- K. Ellmer, *Phys. Stat. Solidi (b)*, 2008, **245**, 1745–1760.
- H. Xu, J. Wu, Q. Feng, N. Mao, C. Wang and J. Zhang, *Small*, 2014, **10**, 2300–2306.
- M. M. Ugeda, A. J. Bradley, Y. Zhang, S. Onishi, Y. Chen, W. Ruan, C. Ojeda-Aristizabal, H. Ryu, M. T. Edmonds, H. Tsai, A. Riss, S.-K. Mo, D. Lee, A. Zettl, Z. Hussain, Z.-X. Shen and M. F. Crommie, *Nat. Phys.*, 2016, **12**, 92–97.
- M. M. Ugeda, A. J. Bradley, S.-F. Shi, F. H. da Jornada, Y. Zhang, D. Y. Qiu, W. Ruan, S.-K. Mo, Z. Hussain, Z.-X. Shen, F. Wang, S. G. Louie and M. F. Crommie, *Nat. Mater.*, 2014, **13**, 1091–1095.
- A. Riss, S. Wickenburg, P. Gorman, L. Z. Tan, H.-Z. Tsai, D. G. de Oteyza, Y.-C. Chen, A. J. Bradley, M. M. Ugeda, G. Etkin, S. G. Louie, F. R. Fischer and M. F. Crommie, *Nano Lett.*, 2014, **14**, 2251–2255.
- S. Jo, N. Ubrig, H. Berger, A. B. Kuzmenko and A. F. Morpurgo, *Nano Lett.*, 2014, **14**, 2019–2025.
- B. Mahler, V. Hoepfner, K. Liao and G. A. Ozin, *J. Am. Chem. Soc.*, 2014, **136**, 14121–14127.
- Y. Sang, Z. Zhao, M. Zhao, P. Hao, Y. Leng and H. Liu, *Adv. Mater.*, 2015, **27**, 363–369.
- Z. Xu, Y. Zhang, S. Lin, C. Zheng, Y. L. Zhong, X. Xia, Z. Li, P. J. Sophia, M. S. Fuhrer, Y. Cheng and Q. Bao, *ACS Nano*, 2015, **9**, 6178–6187.
- Z. Chu, J. Liu, Z. Guo and H. Zhang, *Opt. Mater. Express*, 2016, **6**, 2374–2379.
- C. Wei, H. Luo, H. Zhang, C. Li, J. Xie, J. Li and Y. Liu, *Laser Phys. Lett.*, 2016, **13**, 105108.
- P. Yan, A. Liu, Y. Chen, H. Chen, S. Ruan, C. Guo, S. Chen, I. L. Li, H. Yang, J. Hu and G. Cao, *Opt. Mater. Express*, 2015, **5**, 479–489.
- M. Zhang, G. Hu, G. Hu, R. C. T. Howe, L. Chen, Z. Zheng and T. Hasan, *Sci. Rep.*, 2015, **5**, 17482.
- D. Mao, Y. Wang, C. Ma, L. Han, B. Jiang, X. Gan, S. Hua, W. Zhang, T. Mei and J. Zhao, *Sci. Rep.*, 2015, **5**, 7965.
- E. H. Åhlgren, J. Kotakoski and A. V. Krasheninnikov, *Phys. Rev. B*, 2011, **83**, 115424.
- D. Usachov, O. Vilkov, A. Grüneis, D. Haberer, A. Fedorov, V. K. Adamchuk, A. B. Preobrajenski, P. Dudin, A. Barinov, M. Oehzelt, C. Laubschat and D. V. Vyalikh, *Nano Lett.*, 2011, **11**, 5401–5407.
- H. Wang, Q. Wang, Y. Cheng, K. Li, Y. Yao, Q. Zhang, C. Dong, P. Wang, U. Schwingenschlög, W. Yang and X. X. Zhang, *Nano Lett.*, 2012, **12**, 141–144.
- T. Susi, J. Kotakoski, R. Arenal, S. Kurasch, H. Jiang, V. Skakalova, O. Stephan, A. V. Krasheninnikov, E. I. Kauppinen, U. Kaiser and J. C. Meyer, *ACS Nano*, 2012, **6**, 8837–8846.
- D. S. Fox, Y. Zhou, P. Maguire, A. O'Neill, C. ÓCoileáin, R. Gatensby, A. M. Glushenkov, T. Tao, G. S. Duesberg, I. V. Shvets, M. Abid, M. Abid, H. Wu, Y. Chen, J. N. Coleman, J. F. Donegan, and H. Zhang, *Nano Lett.*, 2015, **15**, 5307–5313.
- M. G. Stanford, P. Raj Pudasaini, A. Belianinov, N. Cross, J. Hyon Noh, M. R. Koehler, D. G. Mandrus, G. Duscher, A. J. Rondinone, I. N. Ivanov, T. Zac Ward and P. D. Rack, *Sci. Rep.*, 2016, **6**, 30481.
- V. Ileri, L. Liang, A. V. Ievlev, M. G. Stanford, M. Lin, X. Li, M. Mahjouri-Samani, S. Jesse, B. G. Sumpter, S. V. Kalinin, D. C. Joy, K. Xiao, A. Belianinov and O. S. Ovchinnikova, *Sci. Rep.*, 2016, **6**, 27276.
- N. Perea-López, A. L. Elías, A. Berkdemir, A. Castro-Beltran, A. Gutiérrez, H. R. Feng, S. Lv, R. Hayashi, T. López-Urías, F. Ghosh, S. Muchharla, B. Talapatra, S. Terrones and H. Terrones, *M. Photosensor Adv. Funct. Mater.*, 2013, **23**, 5511–5517.
- O. Lehtinen, H. Komsa, A. Pulkin, M. B. Whitwick, M. Chen, T. Lehnert, M. J. Mohn, O. V. Yazyev, A. Kis, U. Kaiser and A. V. Krasheninnikov, *ACS Nano*, 2015, **9**, 3274–3283.
- O. Lehtinen, H. Kotakoski, A. V. Krasheninnikov, A. Tolvanen, K. Nordlund and J. Keinonen, *Phys. Rev. B*, 2010, **81**, 153401.
- M. Ghorbani-Asl, S. Kretschmer, D. E. Spearot and A. V. Krasheninnikov, *2D Mater.*, 2017, **4**, 025078.
- M. Kalbac, O. Lehtinen, A. V. Krasheninnikov and J. Keinonen, *Adv. Mater.*, 2013, **25**, 1004.
- G. J. Spühler, R. Paschotta, R. Fluck, B. Braun, M. Moser, G. Zhang, E. Gini, and U. Keller, *J. Opt. Soc. Am. B*, 1999, **16**, 376–388.
- A. Ramasubramaniam, *Phys. Rev. B* 2012, **86**, 115409.
- H. P. Komsa, A. V. Krasheninnikov, *Phys. Rev. B*, 2012, **86**, 241201.
- D. Y. Qiu, F. H. da Jornada and S. G. Louie, *Phys. Rev. Lett.*, 2013, **111**, 216805.
- M. M. Ugeda, A. J. Bradley, S.-F. Shi, F. H. da Jornada, Y. Zhang, D. Y. Qiu, W. Ruan, S. K. Mo, Z. Hussain, Z.-X. Shen, F. Wang, S. G. Louie and M. F. Crommie, *Nat. Mater.*, 2014, **13**, 1091.
- S. Plimpton, *J. Comput. Phys.*, 1995, **117**, 1–19.
- J. W. Jiang, H. S. Park and T. Rabczuk, *J. App. Phys.*, 2013, **114**, 064307.
- J. F. Ziegler, J. P. Biersack, *Treatise on Heavy-Ion Science: Volume 6: Astrophysics, Chemistry, and Condensed Matter*. Springer, Boston, MA, 1985, pp 93–129.
- K. Nordlund, N. Runeberg and D. Sundholm, *Nucl. Instrum. Meth. B*, 1997, **132**, 45–54.
- Y. Tan, Z. Guo, L. Ma, H. Zhang, S. Akhmaliev, S. Zhou and F. Chen, *Opt. Express*, 2016, **24**, 2858–2866.
- Y. Tan, S. Akhmaliev, S. Zhou and F. Chen, *Opt. Express*, 2014, **22**, 3572–3577.